Acta Materialia 194 (2020) 178–189

Contents lists available at ScienceDirect

Acta Materialia

journal homepage: www.elsevier.com/locate/actamat

Full length article

Large tunable elastocaloric effect in additively manufactured Ni–Ti shape memory alloys

Yuxian Cao[a], Xianglin Zhou[a], Daoyong Cong[a,*], Hongxing Zheng[b], Yihuan Cao[a], Zhihua Nie[c], Zhen Chen[a], Shaohui Li[a], Ning Xu[a], Zhiyong Gao[d], Wei Cai[d], Yandong Wang[a]

[a] Beijing Advanced Innovation Center for Materials Genome Engineering, State Key Laboratory for Advanced Metals and Materials, University of Science and Technology Beijing, Beijing 100083, China
[b] Center for Solidification Technology, School of Materials Science and Engineering, Shanghai University, Shanghai 200444, China
[c] School of Materials Science and Engineering, Beijing Institute of Technology, Beijing 100081, China
[d] School of Materials Science and Engineering, Harbin Institute of Technology, Harbin 150001, China

ARTICLE INFO

Article History:
Received 14 January 2020
Revised 12 March 2020
Accepted 6 April 2020
Available online 10 May 2020

Keywords:
Additive manufacturing
Selective laser melting
Elastocaloric effect
Martensitic transformation
Shape memory alloy

ABSTRACT

High-efficiency elastocaloric refrigeration requires high-performance elastocaloric materials with both large surface areas to promote heat exchange rate and large elastocaloric effects to increase the amount of heat transfer. Ni–Ti shape memory alloys (SMAs) are the most promising elastocaloric materials but they are difficult to process by conventional methods due to their poor manufacturability. Here, we successfully developed Ni–Ti SMAs with large elastocaloric effects by additive manufacturing which has the capability to fabricate complex geometries with large surface areas. The phase transformation temperatures of these additively manufactured Ni–Ti SMAs, fabricated by selective laser melting (SLM), can be tuned by varying the SLM processing parameters and/or post heat treatments and thus tunable large elastocaloric effects were achieved at different temperatures, which can be used for different applications. Owing to its large transformation entropy change and high yield strength as a result of precipitation hardening, the aged SLM fabricated alloy exhibits a remarkably large elastocaloric effect with an adiabatic temperature change as high as 23.2 K, which is among the highest values reported for all Ni–Ti SMAs fabricated by both conventional methods and additive manufacturing. Furthermore, by virtue of the high yield strength and low stress hysteresis of the aged alloy, this large elastocaloric effect shows good stability during cycling. The achievement of such large elastocaloric effects in alloys fabricated by near-net-shape additive manufacturing may accelerate the implementation of high-efficiency elastocaloric refrigeration. This study is instructive for the development of advanced high-performance solid-state refrigeration materials by additive manufacturing.

1. Introduction

Solid-state cooling technology based on caloric effects of materials is a promising alternative to the traditional vapor compression cooling technology that produces ozone-depleting or greenhouse gases, owing to its environmental friendliness and high energy efficiency [1,2]. Recently, a series of caloric effects including electrocaloric effect (induced by electric field) [3], magnetocaloric effect (induced by magnetic field) [4], elastocaloric effect (induced by uniaxial stress) [5] and barocaloric effect (induced by hydrostatic pressure) [6] have been reported. Elastocaloric refrigeration based on the elastocaloric effect [7–14] is considered to be the most promising solid-state cooling technology [15]. The elastocaloric effect is characterized by the adiabatic temperature change ΔT_{ad} and the isothermal entropy change ΔS_{iso} upon the application or removal of a uniaxial stress [16]. Shape memory alloys (SMAs) are excellent elastocaloric candidate materials owing to their superior elastocaloric properties. The elastocaloric effect of SMAs originates from the latent heat associated with the reversible stress-induced martensitic transformation [17–19]. To date, several prototypes of elastocaloric refrigeration systems and devices based on the use of SMAs have already been successfully developed [20–22]. For elastocaloric performance, a large elastocaloric effect is required since it is closely related to the amount of heat transfer. To achieve a high heat exchange rate and cooling efficiency, which is of great importance for practical applications, elastocaloric refrigeration demands materials geometries with large surface areas, and even complex shapes such as honey-comb and mesh shapes are needed [23].

Among all the elastocaloric materials, Ni–Ti SMAs are the most suitable materials for engineering applications of elastocaloric refrigeration, due to their large elastocaloric effect [1], excellent mechanical properties [18,24] and superb corrosion resistance. As a result of the large latent heat associated with reversible martensitic transformation

* Corresponding author.
E-mail address: dycong@ustb.edu.cn (D. Cong).

https://doi.org/10.1016/j.actamat.2020.04.007
1359-6454/

[19], huge elastocaloric effects with a maximum ΔT_{ad} of more than 20 K can be obtained in Ni–Ti SMAs [1,25], which is quite beneficial for elastocaloric refrigeration. In addition, Ni–Ti SMAs display excellent shape memory effect and superelasticity as well as good biocompatibility [18,26,27], and thus show promising prospects for sensing, actuating and biomedical applications [28–30]. However, it is a hard task to fabricate Ni–Ti parts with conventional methods (smelting, cold/hot working and machining) due to their high reactivity, poor machinability and high resistance to deformation [31–33]. Thus, all the conventionally fabricated Ni–Ti parts have simple geometries, which greatly limits the applicability of Ni–Ti SMAs. Moreover, heretofore the huge elastocaloric effects (with ΔT_{ad} above 20 K) are mostly reported in small-size Ni–Ti wires [7] or nanocrystalline Ni–Ti sheets that require very complex thermomechanical processing. It remains a great challenge to acquire bulk Ni–Ti alloys with complex geometries and large elastocaloric effects to fulfill the requirement of efficient elastocaloric cooling.

Additive manufacturing, commonly known as 3D printing, is a transforming technique that enables near-net-shape manufacturing of customized complex internal and external shapes of almost any material and minimization of manufacturing waste, owing to a highly digital approach [34]. For additive manufacturing, the material powders or more rarely a wire is completely melted and then built up layer by layer, according to the CAD model, into complex-shaped parts [35], which provides the highest degree of freedom for shape design. The additive manufacturing techniques include powder-bed-based techniques such as selective laser melting (SLM) [36], selective laser sintering [37] and electron beam melting [38] and flow-based techniques such as laser engineered net shaping [39] and laser solid forming [40], among which the powder-bed-based SLM is an emerging advanced technique with many advantages, such as smooth surface of the product, minimal machining, and full utilization of material [36]. Additive manufacturing of structural materials has been successfully used in many fields, such as aerospace, automotive and dental [41]. Nevertheless, additive manufacturing of functional materials is still in the early stage. Additive manufacturing of SMAs can be classified as 4D printing, since the 3D fabricated SMA components are able to evolve in a predefined manner (such as shape change) with time [42]. Particularly, additive manufacturing provides an ideal technique for fabricating near-net-shape Ni–Ti SMAs with large surface areas and/or complex shapes for efficient heat exchange in elastocaloric refrigeration devices and robust mechanical properties to ensure structural integrity [23], considering the poor manufacturability of Ni–Ti SMAs by conventional methods. Therefore, additive manufacturing of Ni–Ti SMAs has recently attracted great attention [30,31,42–47]. However, there are only very limited studies on the elastocaloric effect of additively manufactured Ni–Ti SMAs [23], in which the elastocaloric effect is significantly lower than that in the conventionally fabricated Ni–Ti SMAs [1]. Moreover, the elastocaloric effect in SLM fabricated Ni–Ti SMAs has never been investigated. It is imperative to develop additively manufactured Ni–Ti SMAs with a large elastocaloric effect that is comparable to the highest values in the conventionally fabricated alloys to accelerate the implementation of high-efficiency elastocaloric refrigeration.

Here, we successfully developed SLM fabricated bulk Ni–Ti SMAs with large elastocaloric effects. The elastocaloric effect in such SLM fabricated alloys is tunable by varying SLM processing parameters and/or post heat treatments, so that large elastocaloric effects can be achieved at different temperatures for different applications. Remarkably, the aged alloy shows a large elastocaloric effect with ΔT_{ad} as high as 23.2 K, which is among the highest values reported for all Ni–Ti SMAs fabricated by both conventional methods and additive manufacturing. Furthermore, this large elastocaloric effect in the aged alloy exhibits good stability during cyclic mechanical tests, owing to the high yield strength and low stress hysteresis of the aged alloy. To our knowledge, this is the first study on the elastocaloric properties of SLM fabricated materials. The present work may pave the way for the development of advanced high-performance materials with large elastocaloric effects and complex geometries by additive manufacturing for high-efficiency solid-state cooling.

2. Materials and methods

Commercial pre-alloyed Ni–Ti powders (with nominal Ni content of 51.4 at.%) manufactured by the supreme-speed plasma rotating electrode process were used as the starting materials for SLM fabrication. As determined from the scanning electron microscopy (SEM) micrographs (see Fig. 1a and b), the size of the powders is between 30 and 45 μm. Additively manufactured Ni–Ti alloys were fabricated with a commercial SLM system (SLM-YZ250) equipped with a 500 W Ytterbium fiber laser. This SLM system can be used to fabricate multiple samples at the same time by creating a CAD model. According to the CAD model the Ni–Ti samples were built up layer by layer on a Ti substrate. To prevent oxidation during fabrication, the SLM process is carried out under the argon atmosphere with an oxygen level lower than 100 ppm. The bidirectional scanning strategy was employed; the laser scanning direction rotates by 90° between adjacent layers, as shown in Fig. 1c.

The laser energy input or density E, which is the key factor that influences the quality of the SLM fabricated parts, is directly related to the SLM processing parameters [48]:

$$E = p/vh_st \quad (1)$$

where p denotes laser power, v scanning speed, h_s hatch spacing (Fig. 1c) and t layer thickness. In the present work, to study the effect of hatch spacing h_s, different h_s values of 0.04, 0.05, 0.06, 0.07, 0.08 mm were used while the other parameters were held constant (p = 200 W, v = 1500 mm/s, and t = 0.04 mm) because our preliminary investigation showed that with these parameters relatively high-quality samples can be fabricated. The processing parameters for the SLM fabricated samples are summarized in Table 1. Solution treatment (at 1223 K for 12 h followed by water quenching) and ageing (at 723 K for 5 h followed by air cooling) were performed on some of the fabricated samples to investigate the effect of post heat treatment and to tune the mechanical and elastocaloric properties.

The phase identification was performed at room temperature using X-ray diffraction (XRD) with Cu Kα radiation. The phase transformation temperatures were determined by differential scanning calorimetry (DSC, NETZSCH DSC 214 Polyma) with heating and cooling rates of 10 K/min. The microstructure was examined using a ZEISS optical microscope. The crystallographic orientation and elemental distribution were investigated by electron backscatter diffraction (EBSD) and energy dispersive spectroscopy (EDS) analysis, respectively, using SEM (ZEISS SUPRA55). The precipitates in the aged samples were studied by transmission electron microscopy (TEM, TecnaiF20) operated under an accelerating voltage of 200 kV.

The mechanical properties and elastocaloric effect of the SLM fabricated samples were studied by compression tests using a mechanical testing machine (Instron 5966). The directly fabricated samples ($\Phi 3 \times 6$ mm^3), without any further machining, were used. The stress-strain curves were measured with a low strain rate of 10^{-4} s^{-1}. To ensure the accuracy and reliability of the data, a non-contacting video extensometer was used to record the strain. For the elastocaloric effect measurements, the sample temperature variation during loading and unloading was monitored by a K-type thermocouple attached to the sample surface. The temperature data were recorded by the OM-DAQ-USB-2401 data acquisition module. A relatively high strain rate was used for unloading to approach the adiabatic condition.

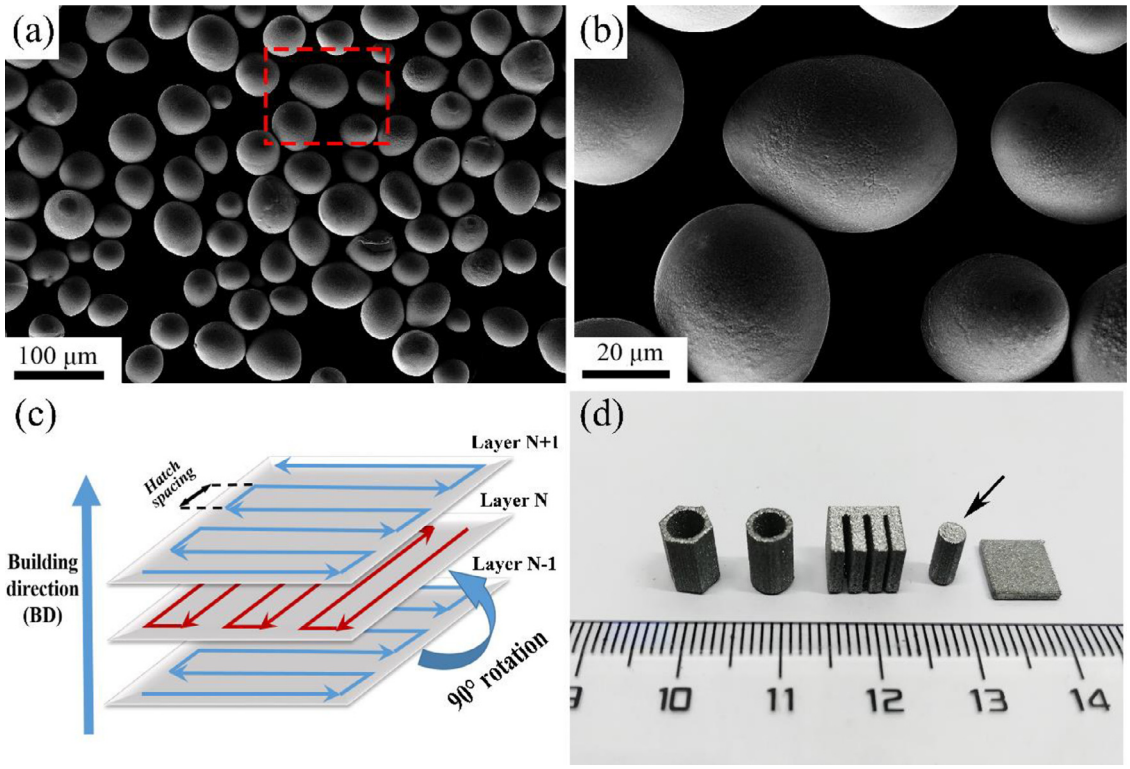

Fig. 1. (a) SEM secondary electron micrograph for Ni–Ti powders. (b) Magnified view of the area enclosed by the dashed frame in (a). (c) Schematic illustration of the bidirectional scanning strategy, with the scanning direction rotating by 90° between adjacent layers. (d) Photographs of the as-fabricated Ni–Ti parts with different geometries (manufactured with h_s = 0.08 mm). The rod indicated by the arrow was used for mechanical and elastocaloric measurements.

3. Results

Typical SLM fabricated Ni–Ti parts are demonstrated in Fig. 1d. As can be seen, various parts with different geometries, some of which have large surface areas beneficial for enhancing heat exchange capability in elastocaloric refrigeration, can be successfully fabricated with SLM. The density of these SLM fabricated parts (with h_s = 0.08 mm) was determined based on Archimedes' Principle and it was found that the ratio of the density of the SLM fabricated parts and that of the conventionally melted alloys was 99.3 ± 0.2%. This suggests that nearly fully dense Ni–Ti parts can be fabricated. In principle, more complex-shaped samples can be manufactured by SLM, owing to the high flexibility in shape design with the digital approach. For easy investigation of the mechanical and elastocaloric properties, we will focus on the rod samples in the following. It is expected that the samples with other geometries show the same properties as those of the rod samples provided that the processing parameters are the same, because they were fabricated with the same technique.

To demonstrate the effect of hatch spacing h_s and post heat treatments on phase transformation, Fig. 2a–c shows the DSC curves for the as-fabricated, solution-treated (1223 K, 12 h) and aged (723 K, 5 h) Ni–Ti alloys manufactured with different h_s, respectively. As can be seen, all the samples exhibit reversible martensitic transformation. The as-fabricated (Fig. 2a) and solution-treated (Fig. 2b) samples exhibit one-step transformation during both cooling and heating, but the aged samples display two-step transformations during cooling and one-step transformation during heating. To gain insights into the transformation sequence, we performed room-temperature XRD experiments on the as-fabricated, solution-treated and aged samples, and the representative results for the samples manufactured with h_s = 0.08 mm are shown in Fig. 3. As indicated from Fig. 3, for the as-fabricated sample, the main phase at room temperature is B2 austenite, but there is also a small amount of B19′ martensite present. For the solution-treated sample, there is only B2 austenite at room temperature. For the aged sample, B2 austenite and R phase coexist at room temperature. The above XRD results suggest that the one-step transformation in the as-fabricated and solution-treated samples is B2 ↔ B19′ and the two-step transformations during cooling and the one-step transformation during heating in the aged sample correspond to B2 → R → B19′ and B19′ → B2, respectively, consistent with the transformation sequences for the solution-treated and aged Ni–Ti alloys reported in the literature [24,49,50].

As indicated from Fig. 2a, the phase transformation temperatures of the as-fabricated samples decrease significantly with increasing h_s. Since elastocaloric effect occurs only above the austenite transformation finish temperature A_f, special attention was paid to the variation of A_f as a function of h_s, which is presented in Fig. 2d. For the solution-treated samples (Fig. 2b), A_f also decreases with increasing h_s

Table 1
Processing parameters for the SLM fabricated Ni–Ti samples.

Sample	Laser power p (W)	Scanning speed v (mm/s)	Hatch spacing h_s (mm)	Layer thickness t (mm)	Energy input E (J/mm^3)
S1	200	1500	0.08	0.04	41.67
S2	200	1500	0.07	0.04	47.62
S3	200	1500	0.06	0.04	55.56
S4	200	1500	0.05	0.04	66.67
S5	200	1500	0.04	0.04	83.33

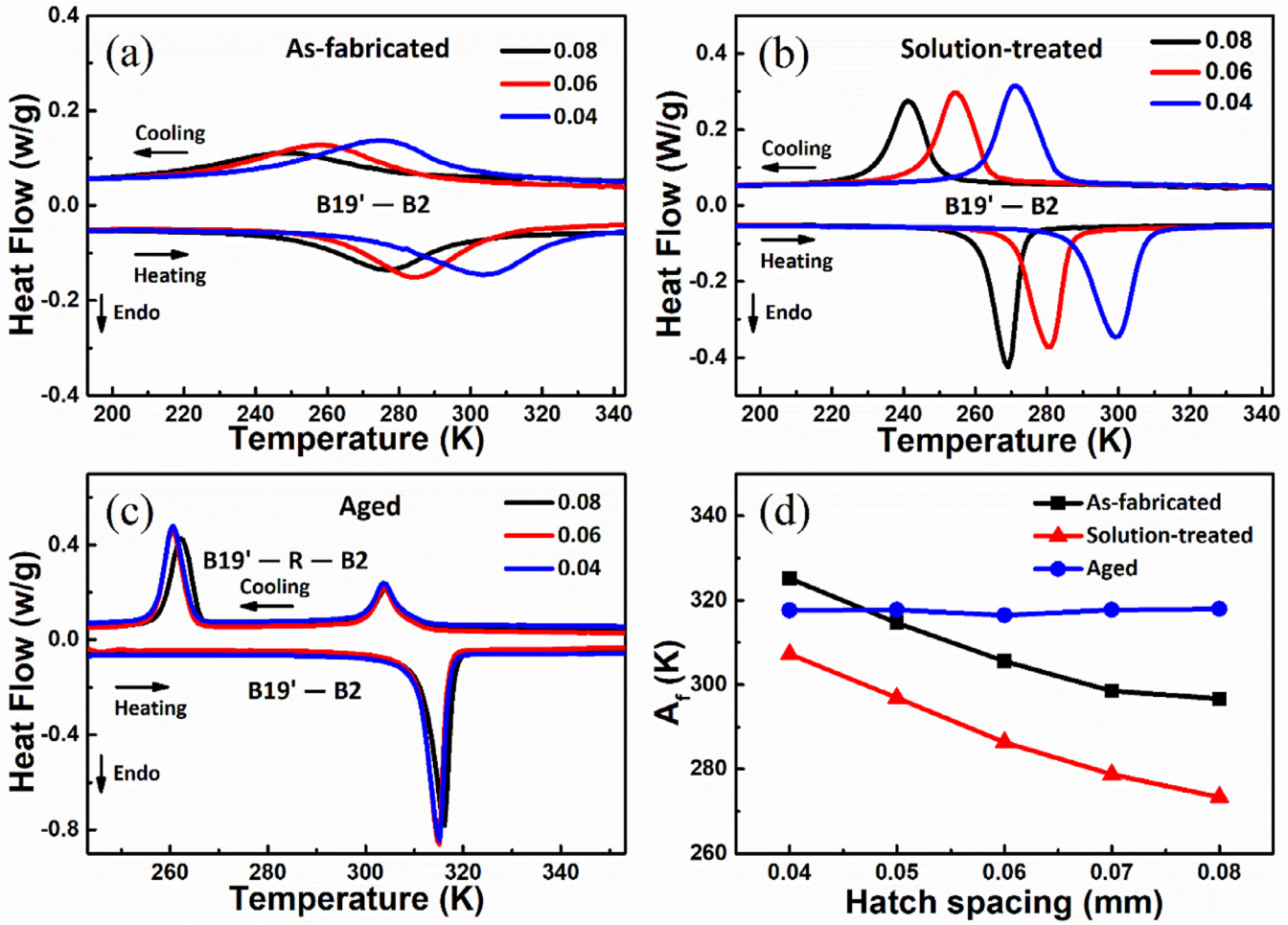

Fig. 2. (a–c) DSC curves of the (a) as-fabricated, (b) solution-treated and (c) aged Ni–Ti alloys manufactured with different hatch spacing h_s of 0.04, 0.06 and 0.08 mm. (d) Austenite transformation finish temperature A_f as a function of hatch spacing h_s for the as-fabricated, solution-treated and aged Ni–Ti alloys.

(Fig. 2d). Nevertheless, for the aged samples (Fig. 2c), A_f remains almost unchanged as h_s increases (Fig. 2d). When comparing Fig. 2a and 2b, one can see that for the samples manufactured with the same h_s, the DSC peaks for the as-fabricated sample are much broader (Fig. 2a) and they become sharpened after solution treatment (Fig. 2b). In addition, A_f decreases after solution treatment (Figs. 2a, 2b, and 2d). After subsequent ageing, A_f increases (compare Fig. 2b and 2c) but the extent to which A_f increases is different for the samples manufactured with different h_s (Fig. 2d). This eventually leads to the fact that the aged samples manufactured with different h_s exhibit almost the same A_f (Fig. 2c and 2d). As is well known, the transformation entropy change (ΔS) is closely related to the magnitude of elastocaloric effect [10], and it can be determined from the DSC peaks with the following relation [51]: $\Delta S \approx \Delta H/T_0$ where, for the reverse transformation, T_0 is the austenite transformation peak temperature and ΔH is the transformation enthalpy change that can be extracted from the area under the endothermic peak. It is found that for the as-fabricated, solution-treated and aged samples, ΔS almost does not change with the variation of h_s; all the samples exhibit a large ΔS, in the range of 55–80 J kg^{-1} K^{-1}. For the samples manufactured with the same h_s, ΔS increases after solution treatment and decreases after subsequent ageing. As an example, the ΔS of the reverse transformation for the as-fabricated, solution-treated and aged samples manufactured with h_s = 0.08 mm is 55, 75 and 64 J kg^{-1} K^{-1}, respectively. As demonstrated above, the phase transformation temperatures of the SLM fabricated samples can be tuned by varying processing parameters and/or post heat treatments, and thus tunable elastocaloric effects can be expected at different temperatures for different applications. The underlying mechanisms responsible for the effect of processing parameters and heat treatments on phase transformation will be discussed later.

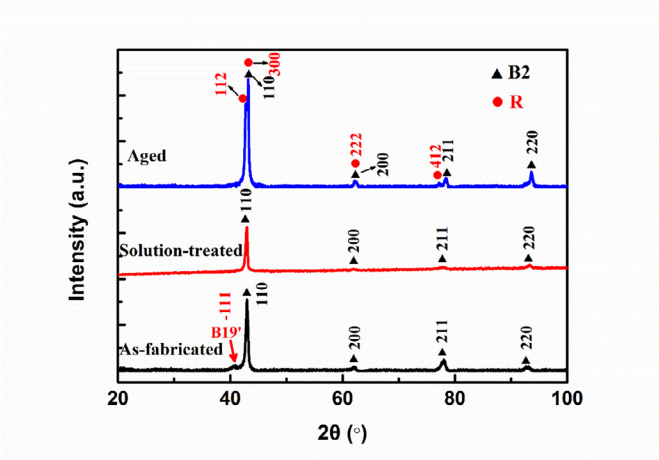

Fig. 3. Room-temperature XRD patterns for the as-fabricated, solution-treated and aged Ni–Ti alloys manufactured with h_s = 0.08 mm.

Fig. 4 shows the optical micrographs of the as-fabricated Ni–Ti alloys manufactured with different h_s of 0.08, 0.06 and 0.04 mm. As seen from Fig. 4a–c, square-shaped grain structure was formed in

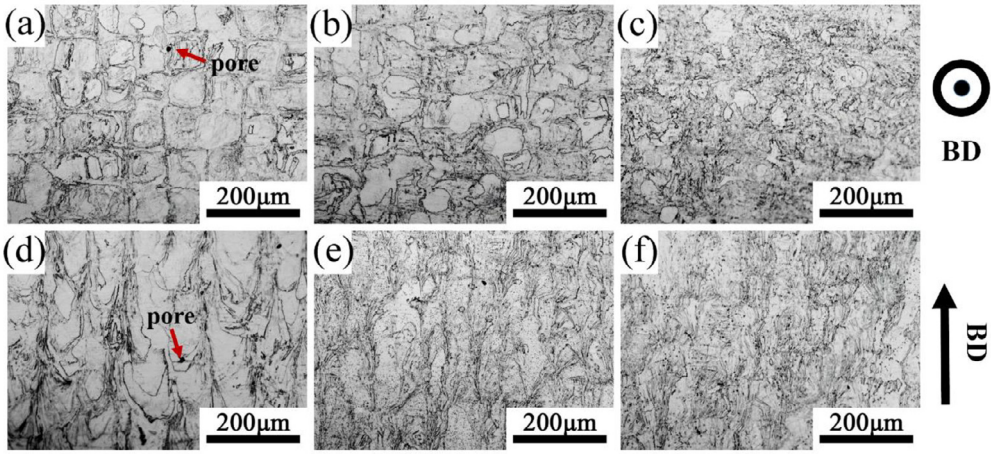

Fig. 4. Optical micrographs for the as-fabricated Ni–Ti alloys manufactured with different hatch spacing h_s of (a, d) 0.08 mm, (b, e) 0.06 mm and (c, f) 0.04 mm. (a–c) were taken in the cross section which is perpendicular to the building direction (BD) and (d–e) were taken in the longitudinal plane which is parallel to the building direction (BD).

the cross section due to the rotation of laser scanning direction by 90° between adjacent layers and the size of the squares is closely related to the h_s. The micrographs taken in the longitudinal plane (Fig. 4d–f) indicate columnar grain structure along the building direction (BD), which is formed as a result of the "epitaxial solidification" that involves the complete melting of the deposited powder layer and the partial re-melting of the previously melted layer [47,52]. Overall, the grain structure demonstrated in Fig. 4 well reflects the scanning path of the SLM fabrication. As shown in Fig. 4, there are very few pores in the samples manufactured with these h_s values. Actually, our measurements based on Archimedes' Principle indicated that the ratio of the density of the SLM fabricated Ni–Ti alloys manufactured with $0.04 \leq h_s \leq 0.08$ mm and that of the conventionally melted alloys is always higher than 99%, indicating that almost fully dense samples can be fabricated with $0.04 \leq h_s \leq 0.08$ mm. We also tried to fabricate samples with h_s = 0.09 mm but it was found that the porosity became higher. To meet the requirements of high quality and fast fabrication for practical applications, here h_s = 0.08 mm is considered as the optimal processing parameter for SLM fabrication. Therefore, we will focus on the alloy fabricated with h_s = 0.08 mm in the following.

To examine the microstructure and crystallographic orientation of the samples subjected to different heat treatments, we performed EBSD measurements. Fig. 5 shows the EBSD orientation maps taken in the longitudinal plane for the as-fabricated, solution-treated and aged samples fabricated with h_s = 0.08 mm. These orientation maps are presented in inverse pole figure mode with respect to the building direction (BD). As seen from Fig. 5a, the as-fabricated sample shows apparent columnar grains in the re-melting region which are enveloped by some fine, slim and diverse grains. After solution treatment, the size of grains increases due to grain growth and the characteristic of columnar grain structure remains (Fig. 5b). Upon subsequent ageing, the grain structure remains essentially unchanged (Fig. 5c). As seen from the inverse pole figures for BD shown in the insets of Fig. 5a–c, there is only weak texture with [001] parallel to BD in the as-fabricated, solution-treated and aged samples.

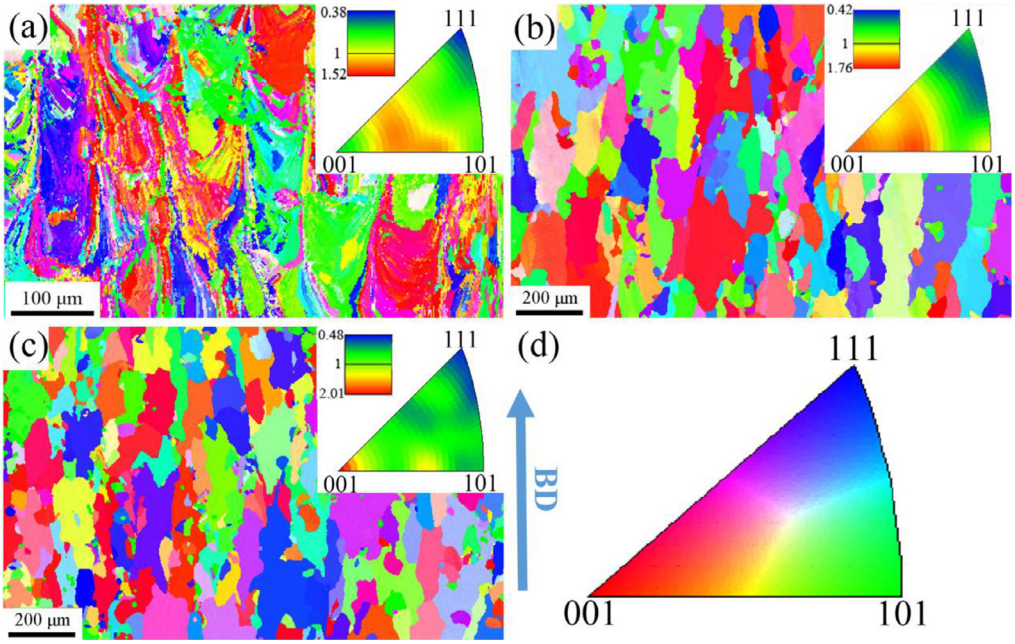

Fig. 5. EBSD orientation maps taken in the longitudinal plane for the (a) as-fabricated, (b) solution-treated and (c) aged Ni–Ti alloys manufactured with h_s = 0.08 mm. These maps are presented in inverse pole figure mode and the legend, which is parallel to the building direction (BD), is displayed in (d). The insets of (a–c) are the corresponding inverse pole figures for the building direction (BD).

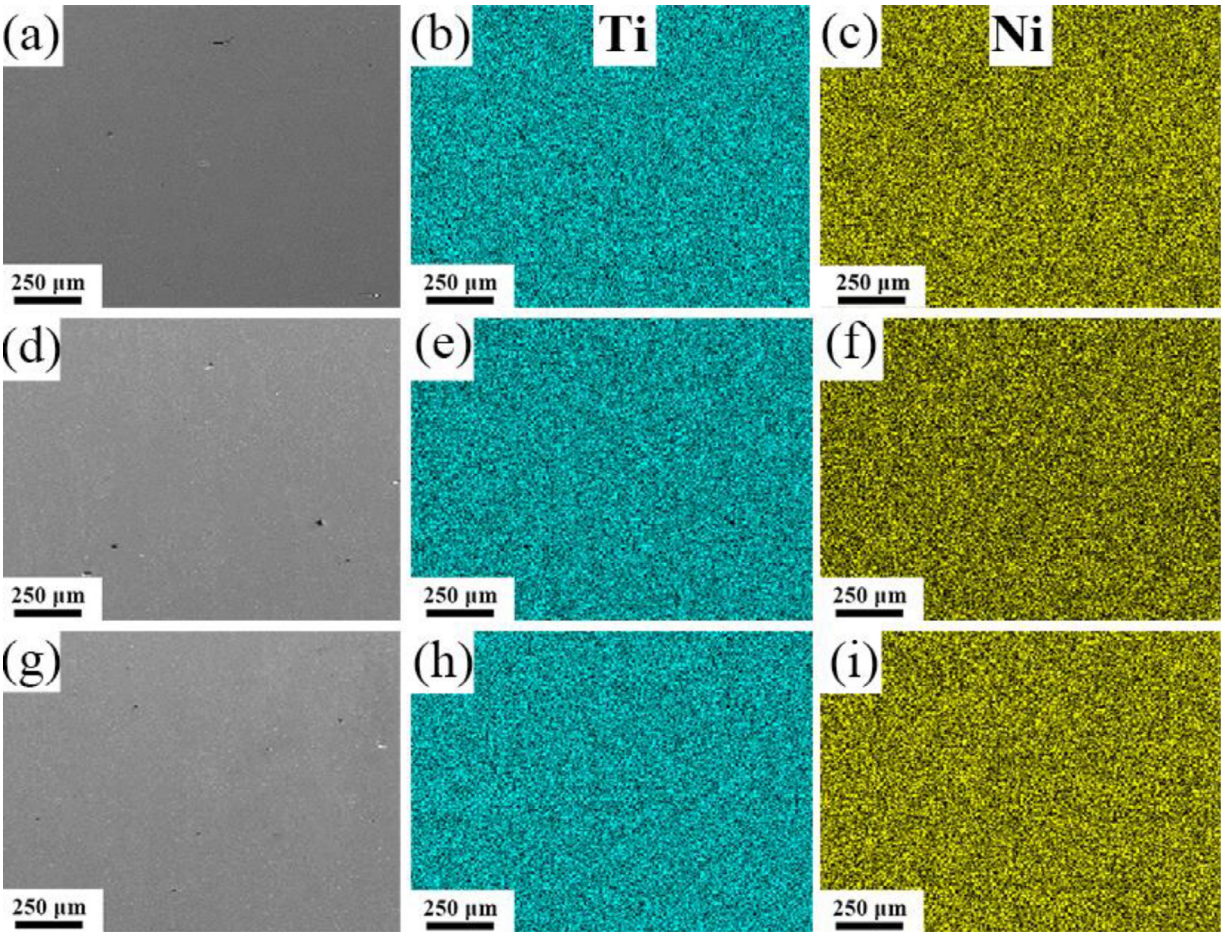

Fig. 6. (a, d, g) SEM secondary electron images and (b, c, e, f, h, i) corresponding EDS maps of the elements Ti and Ni for the (a, b, c) as-fabricated, (d, e, f) solution-treated and (g, h, i) aged Ni–Ti alloys manufactured with h_s = 0.08 mm.

EDS measurements were carried out to check the chemical homogeneity in the SLM fabricated samples. Fig. 6 shows the SEM images and corresponding EDS maps of the elements Ni and Ti for the as-fabricated, solution-treated and aged samples fabricated with h_s = 0.08 mm. As can be seen, for all the samples (as-fabricated, solution-treated and aged), the Ni and Ti elements are almost uniformly distributed and there is no pronounced elemental segregation at the micrometer scale.

Since precipitation usually occurs during ageing in Ni-rich Ni–Ti alloys and the precipitates have pronounced influence on mechanical properties, TEM observation was conducted on the aged sample fabricated with h_s = 0.08 mm to get insights into the size and distribution of precipitates. As seen from the TEM bright field image in Fig. 7a and the high angle annular dark field scanning transmission electron microscopy (HAADF STEM) image in Fig. 7b, nanoscale fine precipitates are randomly dispersed in the matrix. STEM-EDS analysis revealed that the composition of these nanoscale precipitates is very close to Ni_4Ti_3. In fact, these Ni_4Ti_3 precipitates have a lenticular, disc-like shape [24]. As seen from Fig. 7a and b, the size of these Ni_4Ti_3 precipitates is below 80 nm. To check the elemental distribution at the nanometer scale, STEM-EDS mapping was performed and the results are shown in Fig. 7c and d. Since the difference in composition between the Ni_4Ti_3 precipitates and the matrix is not that significant and the Ni_4Ti_3 precipitates are small, the Ni_4Ti_3 precipitates cannot be clearly discerned from the EDS maps. As seen from Fig. 7c and d, the matrix shows a relatively uniform elemental distribution at the nanometer scale.

To investigate the superelastic properties of the samples subjected to different heat treatments, compressive stress–strain curves were measured at a constant temperature (i.e. room temperature for the as-fabricated and solution-treated samples and about 333 K for the aged sample) above the A_f of the samples and the results are shown in Fig. 8. A low strain rate of 10^{-4} s^{-1} was used to ensure the isothermal condition during the measurements. Fig. 8a shows the stress–strain curves recorded during the first loading-unloading cycle. As can be seen, the as-fabricated, solution-treated and aged samples (manufactured with h_s = 0.08 mm) all display superelasticity as a result of stress-induced martensitic transformation. For the as-fabricated and solution-treated samples, the strain cannot be fully recovered and there remains some residual strain after unloading. Noteworthily, the aged sample exhibits perfect superelasticity with a fully recoverable strain of 4.6%, indicating that the stress-induced martensitic transformation in the aged sample is fully reversible. It should be mentioned that the strain was recorded with a non-contacting video extensometer which ensures the accuracy and reliability of the measured strain. The fact that when the maximum applied stress is 960 MPa the strain is still fully recoverable after unloading indicates that there is no permanent plastic deformation by dislocation slip during loading and thus the yield strength of the aged sample is higher than 960 MPa. Among the samples subjected to different heat treatments, the aged sample shows the minimum stress hysteresis (which is about 140 MPa, as determined from the middle of the hysteresis loop). The low stress hysteresis is beneficial for achieving high energy conversion efficiency and good functional stability.

We also examined the cyclic stability of the superelastic response using new samples that have not been tested. Since the functional properties (e.g. superelasticity and elastocaloric effect) of SMAs usually deteriorate most in the first several cycles, we performed cyclic

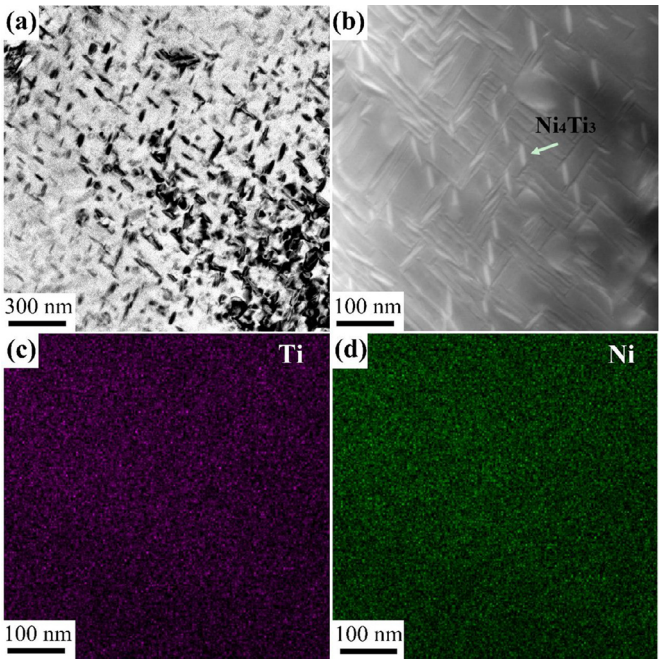

Fig. 7. (a) TEM bright field image, (b) high angle annular dark field scanning transmission electron microscopy (HAADF STEM) image and (c, d) corresponding EDS maps of the elements Ti and Ni taken from the area in (b), for the aged Ni–Ti alloy manufactured with h_s = 0.08 mm.

loading-unloading tests for 10 cycles. As seen from Fig. 8b and c, for the as-fabricated and solution-treated samples, the residual strain becomes smaller and the critical stress for stress-induced martensitic transformation and stress hysteresis decrease rapidly during the first five cycles. Starting from the sixth cycle, the strain becomes almost fully recoverable, indicating that the stress-induced martensitic transformation becomes almost fully reversible, and the critical stress and stress hysteresis tend to be stable. The stress hysteresis during the 10th loading-unloading cycle becomes ~150 MPa for the as-fabricated sample and ~165 MPa for the solution-treated sample. Remarkably, the aged sample exhibits almost stable superelastic response with full strain recovery during 10 cycles of loading and unloading (Fig. 8d); the critical stress for stress-induced martensitic transformation and stress hysteresis show little change during cycling.

The elastocaloric effect of the as-fabricated, solution-treated and aged samples manufactured with h_s = 0.08 mm was studied by monitoring the sample temperature variation during loading and unloading. The test temperature is room temperature for the as-fabricated and solution-treated samples and about 333 K for the aged sample, above the A_f of the samples. Since refrigeration employs the heat absorption process during the transformation from stress-induced martensite to austenite upon unloading, we pay special attention to the adiabatic temperature change (ΔT_{ad}) during unloading. Thus, a relatively high strain rate was applied for unloading, to approximate the adiabatic condition. For each of the as-fabricated, solution-treated and aged samples, we performed elastocaloric measurements during 10 cycles of loading and unloading, and typical results are shown in

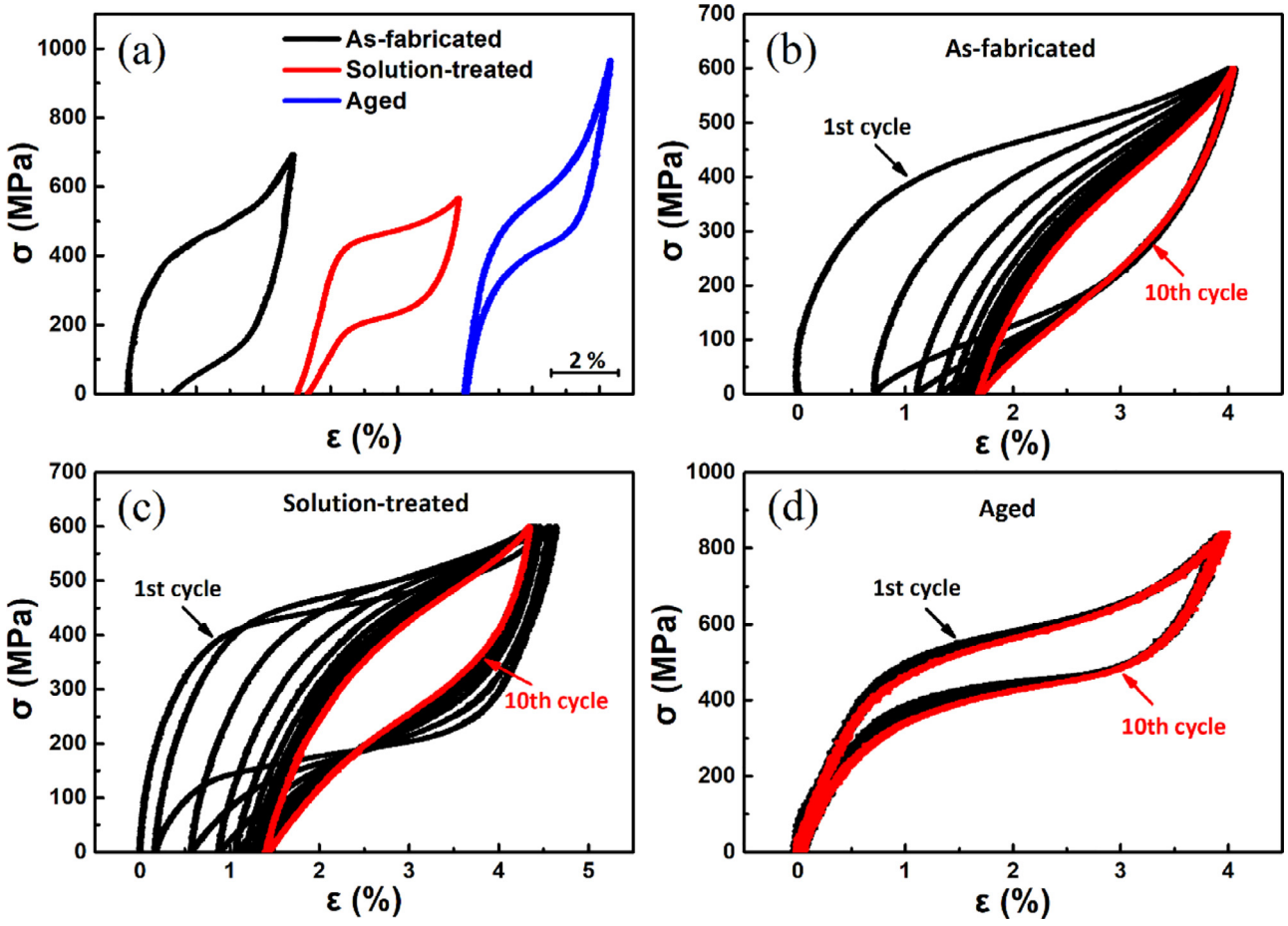

Fig. 8. (a) Stress–strain curves recorded during the first cycle of loading and unloading for the as-fabricated, solution-treated and aged Ni–Ti alloys manufactured with h_s = 0.08 mm. (b–d) Stress–strain curves recorded during 10 cycles of loading and unloading for the (b) as-fabricated, (c) solution-treated and (d) aged Ni–Ti alloys manufactured with h_s = 0.08 mm. For (a)–(d), the curves for the as-fabricated and solution-treated alloys were recorded at room temperature and those for the aged alloy were recorded at about 333 K.

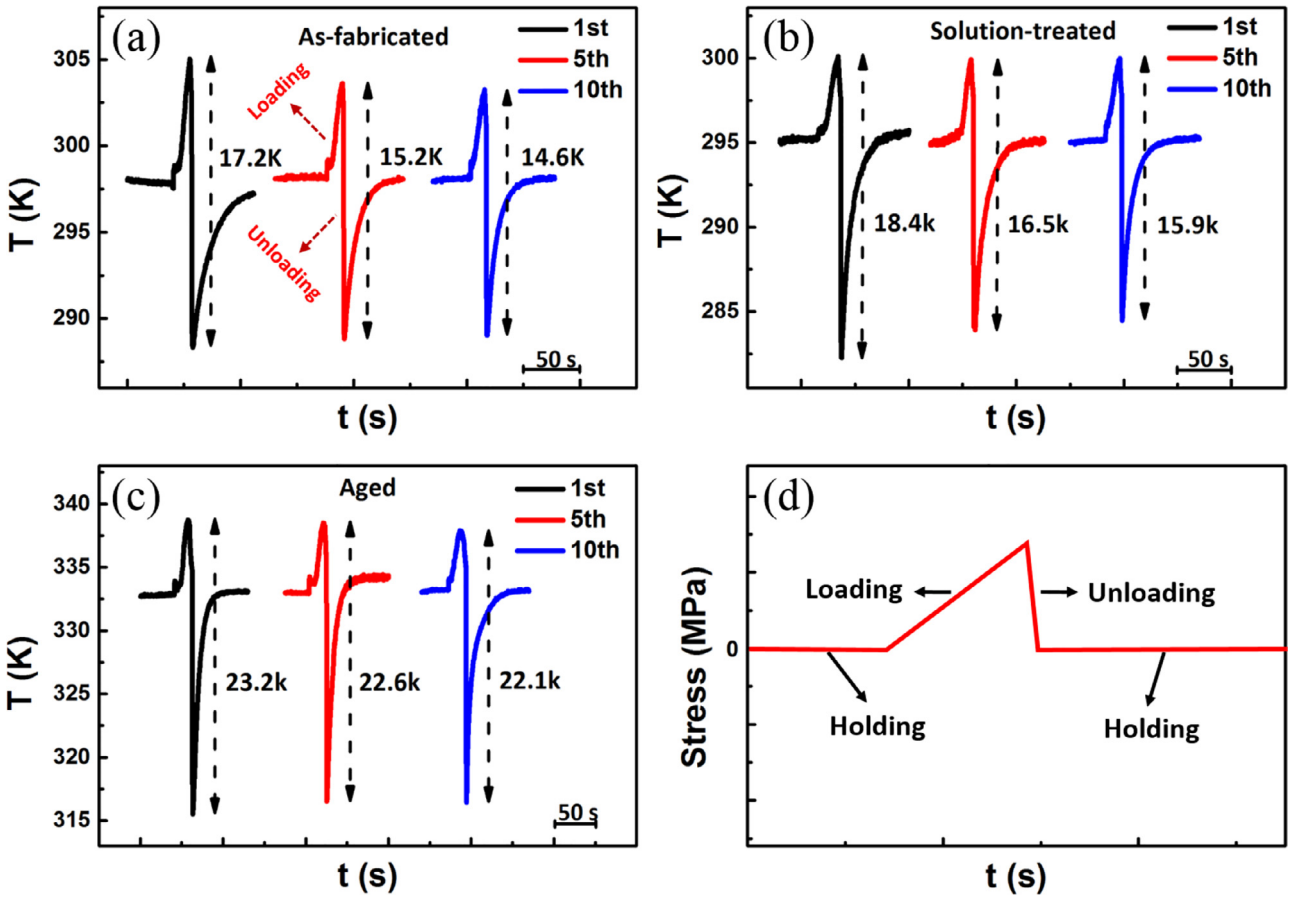

Fig. 9. (a-c) Temperature variation during the 1st, 5th and 10th cycles of loading (with a strain rate of 10^{-3} s^{-1}), unloading (with a strain rate of 6 s^{-1}) and holding, shown as a function of time, for the (a) as-fabricated, (b) solution-treated and (c) aged Ni–Ti alloys manufactured with h_s = 0.08 mm. The maximum applied stress is 550 MPa for the as-fabricated and solution-treated alloys and 750 MPa for the aged alloy. The adiabatic temperature change ΔT_{ad} is indicated in the figures. (d) Schematic illustration of the loading-unloading procedure.

Fig. 9a–c. For each cycle, after initial holding the sample was loaded with a strain rate of 10^{-3} s^{-1} to the maximum stress (which is 550 MPa for the as-fabricated and solution-treated samples and 750 MPa for the aged sample) and then the sample was rapidly unloaded (with a strain rate of 6 s^{-1}) to zero stress followed by further holding (see Fig. 9d for the loading-unloading procedure). It should be noted that no prior training was performed before the elastocaloric measurements.

As seen from the sample temperature *vs.* time profiles shown in Fig. 9a–c, the as-fabricated, solution-treated and aged samples all show a large elastocaloric effect during unloading. The ΔT_{ad} during unloading, which is indicated in the figures, is 17.2 K for the as-fabricated sample (Fig. 9a) and 18.4 K for the solution-treated sample (Fig. 9b) in the first cycle. Remarkably, the aged alloy shows a ΔT_{ad} of as high as 23.2 K in the first cycle. As the number of cycle increases, the ΔT_{ad} for the as-fabricated and solution-treated samples slightly decreases, and the ΔT_{ad} in the 10th cycle becomes 14.6 K and 15.9 K for the as-fabricated sample and the solution-treated sample, respectively. Notably, the large elastocaloric effect in the aged alloy exhibits good stability during the cyclic tests. The ΔT_{ad} for the aged sample is 22.1 K in the 10th cycle and the degradation is less than 5%. As demonstrated above, large tunable elastocaloric effects are achieved at different temperatures (room temperature for the as-fabricated and solution-treated alloys and about 333 K for the aged alloy) in the SLM fabricated Ni–Ti alloys manufactured with h_s = 0.08 mm. Actually, we also examined the elastocaloric effects in the alloys manufactured with other h_s values. As an example, the results for those manufactured with h_s = 0.06 mm are shown in Fig. S1 (Supplementary Information). Evidently, large elastocaloric effects, with ΔT_{ad} values similar to those in the alloys manufactured with h_s = 0.08 mm, are achieved at 310 K in the as-fabricated and solution-treated alloys manufactured with h_s = 0.06 mm (it is worth mentioning that the A_f of the as-fabricated and solution-treated alloys manufactured with h_s = 0.06 mm is higher than that of the corresponding alloys manufactured with h_s = 0.08 mm, as shown in Fig. 2). This confirms that the large elastocaloric effects can indeed be tuned by varying SLM processing parameters.

4. Discussion

4.1. Effect of processing parameters and post heat treatments on phase transformation

As mentioned earlier, to study the effect of hatch spacing h_s, different h_s values were used to fabricate Ni–Ti SMAs while the other parameters were held constant: p = 200 W, v = 1500 mm/s, and t = 0.04 mm. According to Eq. (1), the laser energy density decreases with increasing h_s (Table 1). It was found that almost fully dense samples can be fabricated with $0.04 \leq h_s \leq 0.08$ mm. When h_s is higher than 0.08 mm, the porosity of the fabricated samples becomes high and the density is low. On the other hand, when h_s is lower than 0.04 mm, it is difficult to obtain high-quality samples because of the balling effect that is caused by the excessive energy density at low h_s [53]. Meanwhile, the higher energy density at lower h_s leads to higher temperature of the melt pool and lower solidification rate, which results in more impurities [33]. Therefore, suitable processing

parameters with $0.04 \leq h_s \leq 0.08$ mm are crucial to the high quality of the SLM fabricated samples. Actually, these SLM processing parameters (Table 1) are close to those used for fabricating high-quality Ni–Ti parts in earlier works [47,54,55], i.e. p = 250 W, v = 1100 mm/s, h_s = 0.06 mm and t = 0.03 mm in Ref. [54], p = 250 W, v = 1250 mm/s, h_s = 0.12 mm and t = 0.03 mm in Ref. [55], and p = 200 W, v = 1000 mm/s, h_s = 0.12 mm and t = 0.03 mm in Ref. [47].

Previous studies have discussed the effect of processing parameters [33,47,54,56–58], especially h_s [54,57,58], on the phase transformation of SLM fabricated Ni–Ti alloys. Here we only make a brief discussion. When the laser beam melts the Ni–Ti powders, the high temperature usually leads to Ni loss via evaporation since Ni has a lower evaporation temperature than Ti. With increasing h_s, the energy density decreases and the temperature of the melt pool becomes lower, which results in less Ni evaporation and thus more Ni in the samples. Since the transformation temperatures of Ni-rich Ni–Ti SMAs decrease rapidly with increasing Ni [50], the transformation temperatures of the samples fabricated with higher h_s become lower. This accounts for the significant decrease of A_f with increasing h_s (Fig. 2a and d).

It was reported that Ni-rich secondary phases may form during SLM fabrication of Ni-rich Ni–Ti SMAs [34,59], leading to the decrease of Ni content in the matrix. Moreover, there is inhomogeneous distribution of Ni element and internal stress fields in the as-fabricated samples, which results in the broadening of the phase transformation interval (see the DSC peaks in Fig. 2a) in the as-fabricated samples. During solution treatment which is followed by water quenching, the Ni-rich secondary phases are dissolved into the matrix, leading to the increase of Ni content, the internal stresses are eliminated, and the Ni element becomes homogenously distributed. Therefore, A_f decreases (Fig. 2b and d) and the DSC peaks become sharpened (Fig. 2b) after solution treatment. The dissolution of secondary phases leads to a higher volume fraction of material that participates in martensitic transformation, and thus transformation entropy change ΔS increases after solution treatment. During subsequent ageing, a certain amount of fine Ni-rich Ni_4Ti_3 precipitates form, which results in the decrease of Ni content in the matrix. Therefore, A_f increases after ageing (Fig. 2c and d). As mentioned before, the Ni content is higher in the samples fabricated with higher h_s. During ageing, more Ni_4Ti_3 precipitates form in the samples with higher Ni content. This eventually results in more or less the same Ni content in the matrix of the aged samples manufactured with different h_s. This is why the aged samples manufactured with different h_s have almost the same A_f (Fig. 2c and d). The formation of Ni_4Ti_3 precipitates decreases the volume fraction of material that takes part in martensitic transformation, and hence the ΔS for the reverse transformation decreases after ageing. It should be noted that the ΔS derived from the DSC data for the aged samples is an averaged value for the whole material containing the phase-transforming matrix and the precipitates. Taking into account the HAADF STEM image in Fig. 7b and the values reported in the literature [24,50], the volume fraction of the precipitates in the aged sample manufactured with h_s = 0.08 mm is about 6% and thus the normalized transformation entropy change for the phase-transforming matrix in this sample is 68 J kg^{-1} K^{-1}. The Ni_4Ti_3 precipitates in the aged samples have a size below 80 nm (Fig. 7a and b) and it is usually considered that the Ni_4Ti_3 precipitates with a size below 100 nm are coherent with the matrix [60]. The presence of coherent Ni_4Ti_3 precipitates (Fig. 7a and b) favors the formation of R phase [18,24,50], and this is why there are two-step B2 → R → B19′ transformations during cooling in the aged samples (Fig. 2c), in contrast to the one-step transformation during cooling in the as-fabricated (Fig. 2a) and solution-treated (Fig. 2b) samples. Indeed, the phase transformation can be tuned by varying the SLM fabrication parameters and/or post heat treatments, and this is the basis for obtaining tunable elastocaloric effects in the SLM fabricated Ni–Ti SMAs.

4.2. Effect of post heat treatments on mechanical properties

Superelasticity and elastocaloric effect in SMAs both originate from stress-induced martensitic transformation. If there is no permanent plastic deformation by dislocation slip during stress-induced martensitic transformation, perfect superelasticity and almost reversible temperature changes can be obtained. Owing to the relatively large size of most grains in the as-fabricated and solution-treated samples (Fig. 5a and b), the yield strength of the as-fabricated and solution-treated samples is not very high. During the first loading-unloading cycle, dislocations are created in these samples, leading to permanent plastic deformation, and the dislocation strain field stabilizes some of the stress-induced martensitic variants so that such martensitic variants do not transform back to austenite during unloading [59]. Thus, the strain cannot be fully recovered and there remains some residual strain after unloading in these samples (Fig. 8b and c). Due to the plastic deformation and remnant martensite, the volume fraction of material that takes part in stress-induced martensitic transformation in subsequent loading-unloading cycles becomes lower. The dislocations and remnant martensite generated in the first cycle are located at the “correct” places, creating favorable internal stress for subsequent transformation [10,61] and thus resulting in lower critical stress for stress-induced martensitic transformation in subsequent cycles (Fig. 8b and c). Moreover, the initially generated dislocations and remnant martensite reduce the energy dissipation during transformation, leading to lower stress hysteresis in the following cycles (Fig. 8b and c), and discourage further dislocation formation [10,61]. Thus, fewer and fewer additional dislocations are created during subsequent cycles [62], which results in smaller residual strain in subsequent cycles (Fig. 8b and c), and eventually there are almost no new dislocations generated after a certain number of cycles [62]. This is why starting from the sixth cycle the strain becomes almost fully recoverable and the critical stress and stress hysteresis become nearly stable (Fig. 8b and c).

After ageing, there are nanoscale fine coherent precipitates randomly dispersed in the matrix (Fig. 7a and b). These fine precipitates strongly impede dislocation slip and give rise to pronounced precipitation hardening [33]. Therefore, the yield strength of the aged sample is greatly enhanced. As seen from Fig. 8a, after loading to the maximum stress of 960 MPa, the strain can still be fully recovered after unloading, suggesting that the yield strength of the aged sample is higher than 960 MPa. As a result of the high yield strength, the dislocation generation during stress-induced martensitic transformation is inhibited. Hence, the aged sample shows perfect superelasticity with hardly any irrecoverable strain after unloading (Fig. 8d). Furthermore, the low stress hysteresis of the aged sample leads to low energy dissipation during the stress-induced martensitic transformation and its reverse transformation [61], and reduces the irrecoverable deformation during cycling [62]. Owing to the high yield strength and low stress hysteresis, the aged sample exhibits almost stable superelastic response; the critical stress for martensitic transformation and stress hysteresis remain almost unchanged during cycling (Fig. 8d). Because of the suppression of dislocation generation during stress-induced martensitic transformation, the volume fraction of material participating in the transformation is high and it shows little change during cycling.

4.3. Elastocaloric effect

As mentioned before, the as-fabricated, solution-treated and aged samples all exhibit a large transformation entropy change ΔS; this is one prerequisite for achieving large elastocaloric effects. For the as-fabricated and solution-treated samples, owing to the plastic deformation and stabilized martensite as mentioned above, only part of the stress-induced martensite transforms back to austenite during unloading and the ΔT_{ad} during unloading in the first cycle is 17.2 K

for the as-fabricated sample (Fig. 9a) and 18.4 K for the solution-treated sample (Fig. 9b). The volume fraction of material taking part in the transformation becomes lower as the number of cycle increases and thus the ΔT_{ad} slightly decreases during cycling (Fig. 9a and b). The aged sample exhibits high yield strength which inhibits dislocation generation during stress-induced martensitic transformation, and there is a high volume fraction of material participating in the transformation. Thus, owing to the large ΔS and high yield strength, the aged sample shows a ΔT_{ad} of as high as 23.2 K during unloading in the first cycle (Fig. 9c). By virtue of the high yield strength and low stress hysteresis, the aged alloy shows good elastocaloric stability during cycling (Fig. 9c).

The stress-induced isothermal entropy change ΔS_{iso} is the other important parameter that characterizes the elastocaloric effect. With the stress–strain curves at different temperatures, the ΔS_{iso} can be evaluated based on the integration of the Maxwell relation [5]:

$$\Delta S_{iso} = \frac{1}{\rho}\int_0^{\varepsilon} (\partial\sigma/\partial T)_{\varepsilon} d\varepsilon \quad (2)$$

where ρ is the density which was obtained from our measurements based on Archimedes' Principle. Considering that permanent plastic deformation during stress-induced martensitic transformation occurs in the as-fabricated and solution-treated samples, leading to accumulative irrecoverable strain during successive stress–strain measurements, we only measured the temperature-dependent stress–strain curves of the aged sample. Fig. 10 shows the stress–strain curves measured at different temperatures between 328 K and 348 K for the aged sample. With these stress–strain curves, ΔS_{iso} is estimated numerically. It turns out that the ΔS_{iso} for 4% strain (which is the maximum applied strain in Figs. 8d and 10) at 333 K is 34.9 J kg^{-1} K^{-1}. Actually, this is a large ΔS_{iso} value. With this ΔS_{iso} value, we also attempted to estimate the adiabatic temperature change with the following relation [16]: $\Delta T'_{ad} \approx -T\Delta S_{iso}/C_p$, where C_p is the specific heat capacity which was obtained by our measurement with the modulated DSC technique. $\Delta T'_{ad}$ turns out to be 24.7 K, which is slightly higher than the directly measured ΔT_{ad} (23.2 K). This slight difference might be attributed to the insufficient adiabatic condition. In addition, the presence of Ni_4Ti_3 precipitates may have some influence on the application of the above relation and Eq. (2) for estimation of $\Delta T'_{ad}$ and ΔS_{iso}, but considering the low volume fraction of precipitates the influence is not expected to be significant.

In the present work, large elastocaloric effects are achieved in the SLM fabricated Ni–Ti SMAs. Remarkably, the ΔT_{ad} during unloading in the aged sample is as high as 23.2 K. It is worth mentioning that the rapid cooling and layer-by-layer deposition during SLM fabrication result in specific microstructure (Figs. 4 and 5) with grains much smaller than those in the conventionally cast and heat treated bulk alloys, which is beneficial for improving the yield strength, and, furthermore, the finer grain structure helps promote uniform dispersion of Ni_4Ti_3 precipitates during ageing, which is advantageous for precipitation hardening; thus, the SLM fabricated Ni–Ti SMAs display large elastocaloric effects. To make a comparison between the ΔT_{ad} we achieved in the SLM fabricated Ni–Ti SMAs and that reported in the literature [1,7,22,23,51,63–67], Table 2 lists the ΔT_{ad} during unloading for typical Ni–Ti SMAs. As can be seen, the ΔT_{ad} in our aged SLM fabricated sample is among the highest values reported for all Ni–Ti SMAs fabricated by both conventional methods and additive manufacturing. It is worth noting that the conventionally fabricated Ni–Ti SMAs with large ΔT_{ad} above 20 K are mostly in the form of small-size wires or nanocrystalline thin sheets which require very complex thermomechanical processing and only have simple shapes. In contrast, the sample exhibiting large ΔT_{ad} in the present work was fabricated by additive manufacturing which offers high flexibility in shape design and has the capability to produce complex shapes with large surface areas to boost heat exchange in elastocaloric refrigeration. Meanwhile, additive manufacturing is a near-net-shape forming technology; the manufactured Ni–Ti samples may need post heat treatments but do not need complex cold/hot working and machining, which is quite beneficial especially when considering the poor manufacturability of Ni–Ti SMAs by conventional methods. Furthermore, the large ΔT_{ad} in our present work is achieved in bulk samples, which can be scaled up for large-scale elastocaloric refrigeration applications. More importantly, the elastocaloric effect in the present SLM fabricated alloys is tunable by varying SLM processing parameters and/or post heat treatments, so that large elastocaloric effects can be achieved at different temperatures for different applications. To our knowledge, this is the first study on the elastocaloric effect in SLM fabricated materials and the ΔT_{ad} (23.2 K) we achieved is much higher than that reported in other additively manufactured SMAs.

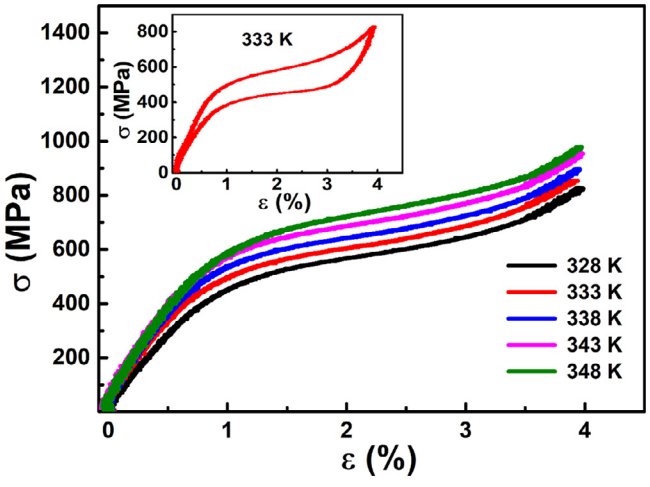

Fig. 10. Stress–strain curves at different temperatures measured with a strain rate of 10^{-4} s^{-1}, for the aged Ni–Ti alloy manufactured with h_s = 0.08 mm. For clarity, only the curves measured during loading are displayed. The inset shows a full stress–strain loop measured at 333 K, as an example.

5. Conclusions

Additively manufactured Ni–Ti SMAs with large elastocaloric effects were successfully developed with the SLM technique. The phase transformation temperatures of such SLM fabricated Ni–Ti SMAs can be tuned by varying the SLM processing parameters and/or post heat treatments, and thereby tunable large elastocaloric effects were achieved at

Table 2
Elastocaloric effect of the present SLM fabricated Ni–Ti and other typical Ni–Ti alloys reported in the literature*.

Alloy	Sample form	Testing temperature (K)	ΔT_{ad} (K)	Reference
SLM Ni–Ti (aged)	bulk pc	333	23.2	This work
SLM Ni–Ti (solution-treated)	bulk pc	295	18.4	This work
SLM Ni–Ti (as-fabricated)	bulk pc	295	17.2	This work
LENS $Ni_{49.8}Ti_{50.2}$	bulk pc	396	7.5	[23]
$Ni_{50.8}Ti_{49.2}$	bulk sc	338	18.2	[64]
$Ni_{48.9}Ti_{51.1}$	wire	330	25	[1]
$Ni_{50}Ti_{50}$	wire	295	17	[7]
$Ni_{50.8}Ti_{49.2}$	wire	294	5.3	[65]
$Ni_{50.4}Ti_{49.6}$	film	300	16	[66]
$Ni_{50.8}Ti_{49.2}$	ribbon	294	14.1	[22]
$Ni_{50.8}Ti_{49.2}$	thin sheet	338	25.3	[51]
$Ni_{50.8}Ti_{49.2}$	thin sheet	298	12	[67]
$Ni_{50.1}Ti_{49.9}$	thin sheet	295	6	[63]

* ΔT_{ad}: directly measured adiabatic temperature change during unloading, pc: polycrystal, sc: single crystal, LENS: laser engineered net shaping. Only the SLM Ni–Ti and LENS $Ni_{49.8}Ti_{50.2}$ were fabricated by additive manufacturing.

different temperatures, which may be used for different applications. Owing to its large transformation entropy change ΔS and high yield strength as a result of precipitation hardening, the aged alloy shows a remarkably large elastocaloric effect with ΔT_{ad} during unloading as high as 23.2 K, which is among the highest values reported for all Ni–Ti SMAs fabricated by both conventional methods and additive manufacturing. Furthermore, this large elastocaloric effect exhibits good cyclic stability, which is attributed to the high yield strength and low stress hysteresis of the aged alloy. The achievement of such large elastocaloric effects in alloys fabricated by near-net-shape additive manufacturing that enables the fabrication of complex shapes with large surface areas to enhance heat exchange capability may push a significant step forward towards high-efficiency elastocaloric cooling applications. This study is instructive for developing high-performance solid-state refrigeration materials by additive manufacturing.

Declaration of Competing Interest

The authors declare that they have no known competing financial interests or personal relationships that could have appeared to influence the work reported in this paper.

Acknowledgments

Financial support from the National Natural Science Foundation of China (Nos. 51731005, 51822102, and 51831003), the Fundamental Research Funds for the Central Universities (No. FRF-TP-18-008C1), and the State Key Laboratory for Advanced Metals and Materials (Grant no. 2019Z-09) is gratefully acknowledged. This work is also supported by the Funds for Creative Research Groups of China (No. 51921001) and the 111 Project (No. B170003).

Supplementary materials

Supplementary material associated with this article can be found, in the online version, at doi:10.1016/j.actamat.2020.04.007.

References

[1] J. Tušek, K. Engelbrecht, R. Millán-Solsona, L. Mañosa, E. Vives, L.P. Mikkelsen, N. Pryds, The elastocaloric effect: a way to cool efficiently, Adv. Energy Mater. 5 (2015) 1500361.
[2] P. Lloveras, E. Stern-Taulats, M. Barrio, J.L. Tamarit, S. Crossley, W. Li, V. Pomjakushin, A. Planes, L. Mañosa, N.D. Mathur, X. Moya, Giant barocaloric effects at low pressure in ferrielectric ammonium sulphate, Nat. Commun. 6 (2015) 8801.
[3] A.S. Mischenko, Q. Zhang, J.F. Scott, R.W. Whatmore, N.D. Mathur, Giant electrocaloric effect in thin-film $PbZr_{0.95}Ti_{0.05}O_3$, Science 311 (2006) 1270–1271.
[4] A.M. Tishin, Y.I. Spichkin, Recent progress in magnetocaloric effect: Mechanisms and potential applications, Int. J. Refrig. 37 (2014) 223–229.
[5] E. Bonnot, R. Romero, L. Mañosa, E. Vives, A. Planes, Elastocaloric effect associated with the martensitic transition in shape-memory alloys, Phys. Rev. Lett. 100 (2008) 125901.
[6] L. Mañosa, D. González-Alonso, A. Planes, E. Bonnot, M. Barrio, J.L. Tamarit, S. Aksoy, M. Acet, Giant solid-state barocaloric effect in the Ni-Mn-In magnetic shape-memory alloy, Nat. Mater. 9 (2010) 478–481.
[7] J. Cui, Y. Wu, J. Muehlbauer, Y. Hwang, R. Radermacher, S. Fackler, M. Wuttig, I. Takeuchi, Demonstration of high efficiency elastocaloric cooling with large ΔT using NiTi wires, Appl. Phys. Lett. 101 (2012) 073904.
[8] L. Mañosa, S. Jarque-Farnos, E. Vives, A. Planes, Large temperature span and giant refrigerant capacity in elastocaloric Cu-Zn-Al shape memory alloys, Appl. Phys. Lett. 103 (2013) 211904.
[9] S.-M. Kirsch, F. Welsch, N. Michaelis, M. Schmidt, A. Wieczorek, J. Frenzel, G. Eggeler, A. Schütze, S. Seelecke, NiTi-based elastocaloric cooling on the macroscale: From basic concepts to realization, Energy Technol. 6 (2018) 1567–1587.
[10] Z. Yang, D.Y. Cong, X.M. Sun, Z.H. Nie, Y.D. Wang, Enhanced cyclability of elastocaloric effect in boron-microalloyed Ni-Mn-In magnetic shape memory alloys, Acta Mater. 127 (2017) 33–42.
[11] E. Vives, S. Burrows, R.S. Edwards, S. Dixon, L. Mañosa, A. Planes, R. Romero, Temperature contour maps at the strain-induced martensitic transition of a Cu–Zn–Al shape-memory single crystal, Appl. Phys. Lett. 98 (2011) 011902.
[12] F. Xiao, T. Fukuda, T. Kakeshita, X. Jin, Elastocaloric effect by a weak first-order transformation associated with lattice softening in an Fe-31.2Pd (at.%) alloy, Acta Mater. 87 (2015) 8–14.
[13] J. Tušek, A. Žerovnik, M. Čebron, M. Brojan, B. Žužek, K. Engelbrecht, A. Cadelli, Elastocaloric effect vs fatigue life: Exploring the durability limits of Ni–Ti plates under pre-strain conditions for elastocaloric cooling, Acta Mater 150 (2018) 295–307.
[14] S. Qian, Y. Geng, Y. Wang, J. Ling, Y. Hwang, R. Radermacher, I. Takeuchi, J. Cui, A review of elastocaloric cooling: materials, cycles and system integrations, Int. J. Refrig. 64 (2016) 1–19.
[15] Energy savings potential and RD&D opportunities for non-vapor-compression HVAC technologies, Report of the U.S, Report of the U.S, 4, Department of Energy, 2014 https://energy.gov/eere/buildings/downloads/non-vapor-compression-hvac-technologies-report .
[16] L. Mañosa, A. Planes, Materials with giant mechanocaloric effects: cooling by strength, Adv. Mater. 29 (2017) 1603607.
[17] C. Chluba, W. Ge, R.L. de Miranda, J. Strobel, L. Kienle, E. Quandt, M. Wuttig, Ultra-low-fatigue shape memory alloy films, Science 348 (2015) 1004–1007.
[18] K. Otsuka, X. Ren, Physical metallurgy of Ti-Ni-based shape memory alloys, Prog. Mater. Sci. 50 (2005) 511–678.
[19] J. Frenzel, A. Wieczorek, I. Opahle, B. Maaß, R. Drautz, G. Eggeler, On the effect of alloy composition on martensite start temperatures and latent heats in Ni–Ti-based shape memory alloys, Acta Mater. 90 (2015) 213–231.
[20] H. Ossmer, F. Wendler, M. Gueltig, F. Lambrecht, S. Miyazaki, M. Kohl, Energy-efficient miniature-scale heat pumping based on shape memory alloys, Smart Mater. Struct. 25 (2016) 085037.
[21] S. Qian, Y. Geng, Y. Wang, J. Muehlbauer, J. Ling, Y. Hwang, R. Radermacher, I. Takeuchi, Design of a hydraulically driven compressive elastocaloric cooling system, Sci. Technol. Built. Eng. 22 (2016) 500–506.
[22] M. Schmidt, A. Schütze, S. Seelecke, Scientific test setup for investigation of shape memory alloy based elastocaloric cooling processes, Int. J. Refrig. 54 (2015) 88–97.
[23] H. Hou, E. Simsek, D. Stasak, N.A. Hasan, S. Qian, R. Ott, J. Cui, I. Takeuchi, Elastocaloric cooling of additive manufactured shape memory alloys with large latent heat, J. Phys. D 50 (2017) 404001.
[24] D.Y. Cong, G. Saha, M.R. Barnett, Thermomechanical properties of Ni–Ti shape memory wires containing nanoscale precipitates induced by stress-assisted ageing, Acta Biomater. 10 (2014) 5178–5192.
[25] H. Chen, F. Xiao, X. Liang, Z. Li, Z. Li, X. Jin, N. Min, T. Fukuda, Improvement of the stability of superelasticity and elastocaloric effect of a Ni-rich Ti-Ni alloy by precipitation and grain refinement, Scr. Mater. 162 (2019) 230–234.
[26] J.M. Jani, M. Leary, A. Subic, M.A. Gibson, A review of shape memory alloy research, applications and opportunities, Mater. Des. 56 (2014) 1078–1113.
[27] S. Saadat, J. Salichs, M. Noori, Z. Hou, H. Davoodi, I. Bar-On, Y. Suzuki, A. Masuda, An overview of vibration and seismic applications of NiTi shape memory alloy, Smart Mater. Struct. 11 (2002) 218–229.
[28] M.T. Andani, N.S. Moghaddam, C. Haberland, D. Dean, M.J. Miller, M. Elahinia, Metals for bone implants. Part 1. Powder metallurgy and implant rendering, Acta Biomater. 10 (2014) 4058–4070.
[29] J. Van Humbeeck, Non-medical applications of shape memory alloys, Mater. Sci. Eng. A 273 (1999) 134–148.
[30] T. Habijan, C. Haberland, H. Meier, J. Frenzel, J. Wittsiepe, C. Wuwer, C. Greulich, T.A. Schildhauer, M. Köller, The biocompatibility of dense and porous nickel-titanium produced by selective laser melting, Mater. Sci. Eng. C 33 (2013) 419–426.
[31] M.H. Elahinia, M. Hashemi, M. Tabesh, S.B. Bhaduri, Manufacturing and processing of NiTi implants: a review, Prog. Mater. Sci. 57 (2012) 911–946.
[32] K. Weinert, V. Petzoldt, Machining of NiTi based shape memory alloys, Mater. Sci. Eng. A 378 (2004) 180–184.
[33] C. Haberland, M. Elahinia, J.M. Walker, H. Meier, J. Frenzel, On the development of high quality NiTi shape memory and pseudoelastic parts by additive manufacturing, Smart Mater. Struct. 23 (2014) 104002.
[34] M. Elahinia, N.S. Moghaddam, M.T. Andani, A. Amerinatanzi, B.A. Bimber, R.F. Hamilton, Fabrication of NiTi through additive manufacturing: a review, Prog. Mater. Sci. 83 (2016) 630–663.
[35] D. Herzog, V. Seyda, E. Wycisk, C. Emmelmann, Additive manufacturing of metals, Acta Mater. 117 (2016) 371–392.
[36] L.C. Zhang, H. Attar, Selective laser melting of titanium alloys and titanium matrix composites for biomedical applications: a review, Adv. Eng. Mater. 18 (2016) 463–475.
[37] J.-P. Kruth, P. Mercelis, J. Van Vaerenbergh, L. Froyen, M. Rombouts, Binding mechanisms in selective laser sintering and selective laser melting, Rapid Prototyp. J. 11 (2005) 26–36.
[38] L.E. Murr, S.M. Gaytan, D.A. Ramirez, E. Martinez, J. Hernandez, K.N. Amato, P.W. Shindo, F.R. Medina, R.B. Wicker, Metal fabrication by additive manufacturing using laser and electron beam melting technologies, J. Mater. Sci. Technol. 28 (2012) 1–14.
[39] R.P. Mudge, N.R. Wald, Laser engineered net shaping advances additive manufacturing and repair, Weld. J. 86 (2007) 44–48.
[40] F. Liu, X. Lin, H. Leng, J. Cao, Q. Liu, C. Huang, W. Huang, Microstructural changes in a laser solid forming Inconel 718 superalloy thin wall in the deposition direction, Opt. Laser Technol. 45 (2013) 330–335.
[41] S.M. Thompson, L. Bian, N. Shamsaei, A. Yadollahi, An overview of direct laser deposition for additive manufacturing; Part I: transport phenomena, modeling and diagnostics, Addit. Manuf. 8 (2015) 36–62.
[42] Z.X. Khoo, J.E.M. Teoh, Y. Liu, C.K. Chua, S. Yang, J. An, K.F. Leong, W.Y. Yeong, 3D printing of smart materials: a review on recent progresses in 4D printing, Virtual Phys. Prototyp. 10 (2015) 103–122.

[43] Z.X. Khoo, Y. Liu, J. An, C.K. Chua, Y.F. Shen, C.N. Kuo, A review of selective laser melted NiTi shape memory alloy, Materials 11 (2018) 519.
[44] T. Bormann, B. Müller, M. Schinhammer, A. Kessler, P. Thalmann, M. de Wild, Microstructure of selective laser melted nickel-titanium, Mater. Charact. 94 (2014) 189–202.
[45] T. Bormann, R. Schumacher, B. Müller, M. Mertmann, M. de Wild, Tailoring selective laser melting process parameters for NiTi implants, J. Mater. Eng. Perform. 21 (2012) 2519–2524.
[46] S. Dadbakhsh, B. Vrancken, J.-P. Kruth, J. Luyten, J. Van Humbeeck, Texture and anisotropy in selective laser melting of NiTi alloy, Mater. Sci. Eng. A 650 (2016) 225–232.
[47] S. Saedi, N.S. Moghaddam, A. Amerinatanzi, M. Elahinia, H.E. Karaca, On the effects of selective laser melting process parameters on microstructure and thermomechanical response of Ni-rich NiTi, Acta Mater. 144 (2018) 552–560.
[48] K.G. Prashanth, S. Scudino, T. Maity, J. Das, J. Eckert, Is the energy density a reliable parameter for materials synthesis by selective laser melting? Mater. Res. Lett. 5 (2017) 386–390.
[49] T. Waitz, V. Kazykhanov, H.P. Karnthaler, Martensitic phase transformations in nanocrystalline NiTi studied by TEM, Acta Mater. 52 (2004) 137–147.
[50] J. Khalil-Allafi, A. Dlouhy, G. Eggeler, Ni_4Ti_3-precipitation during aging of NiTi shape memory alloys and its influence on martensitic phase transformations, Acta Mater. 50 (2002) 4255–4274.
[51] H. Chen, F. Xiao, X. Liang, Z. Li, X. Jin, T. Fukuda, Stable and large superelasticity and elastocaloric effect in nanocrystalline Ti-44Ni-5Cu-1Al (at%) alloy, Acta Mater. 158 (2018) 330–339.
[52] J. Liu, A.C. To, Quantitative texture prediction of epitaxial columnar grains in additive manufacturing using selective laser melting, Addit. Manuf. 16 (2017) 58–64.
[53] D. Gu, Y. Shen, Balling phenomena during direct laser sintering of multi-component Cu-based metal powder, J. Alloy. Compd. 432 (2007) 163–166.
[54] S. Dadbakhsh, M. Speirs, J.-P. Kruth, J. Schrooten, J. Luyten, J. Van Humbeeck, Effect of SLM parameters on transformation temperatures of shape memory nickel titanium parts, Adv. Eng. Mater. 16 (2014) 1140–1146.
[55] S. Saedi, A.S. Turabi, M.T. Andani, C. Haberland, H. Karaca, M. Elahinia, The influence of heat treatment on the thermomechanical response of Ni-rich NiTi alloys manufactured by selective laser melting, J. Alloy. Compd. 677 (2016) 204–210.
[56] S. Dadbakhsh, M. Speirs, J.-P. Kruth, J. Van Humbeeck, Influence of SLM on shape memory and compression behaviour of NiTi scaffolds, CIRP Ann. Manuf. Technol. 64 (2015) 209–212.
[57] N.S. Moghaddam, S. Saedi, A. Amerinatanzi, A. Hinojos, A. Ramazani, J. Kundin, M.J. Mills, H. Karaca, M. Elahinia, Achieving superelasticity in additively manufactured NiTi in compression without post-process heat treatment, Sci. Rep. 9 (2019) 41.
[58] M. Speirs, X. Wang, S. Van Baelen, A. Ahadi, S. Dadbakhsh, J.-P. Kruth, J. Van Humbeeck, On the transformation behavior of NiTi Shape-Memory alloy produced by SLM, Shap. Mem. Superelast. 2 (2016) 310–316.
[59] C. Haberland, H. Meier, J. Frenzel, On the properties of Ni-rich NiTi shape memory parts produced by selective laser melting, in: Proceedings of the ASME 2012 Conference on Smart Materials, Adaptive Structures and Intelligent Systems, 2012, pp. 97–104.
[60] K. Gall, K. Juntunen, H.J. Maier, H. Sehitoglu, Y.I. Chumlyakov, Instrumented micro-indentation of NiTi shape-memory alloys, Acta Mater. 49 (2001) 3205–3217.
[61] J. Ma, I. Karaman, R.D. Noebe, High temperature shape memory alloys, Int. Mater. Rev. 55 (2010) 257–315.
[62] C. Grossmann, J. Frenzel, V. Sampath, T. Depka, G. Eggeler, Elementary transformation and deformation processes and the cyclic stability of NiTi and NiTiCu shape memory spring actuators, Metall. Mater. Trans. A 40 (2009) 2530–2544.
[63] K. Mukherjee, S. Sircar, N.B. Dahotre, Thermal effects associated with stress-induced martensitic transformation in a Ti-Ni alloy, Mater. Sci. Eng. 74 (1985) 75–84.
[64] Y. Wu, E. Ertekin, H. Sehitoglu, Elastocaloric cooling capacity of shape memory alloys −− role of deformation temperatures, mechanical cycling, stress hysteresis and inhomogeneity of transformation, Acta Mater. 135 (2017) 158–176.
[65] X. Liang, F. Xiao, M. Jin, X. Jin, T. Fukuda, T. Kakeshita, Elastocaloric effect induced by the rubber-like behavior of nanocrystalline wires of a Ti-50.8 Ni (at.%) alloy, Scr. Mater. 134 (2017) 42–46.
[66] H. Ossmer, F. Lambrecht, M. Gültig, C. Chluba, E. Quandt, M. Kohl, Evolution of temperature profiles in TiNi films for elastocaloric cooling, Acta Mater. 81 (2014) 9–20.
[67] J. Tušek, K. Engelbrecht, D. Eriksen, S. Dall'Olio, J. Tušek, N. Pryds, A regenerative elastocaloric heat pump, Nat. Energy 1 (2016) 16134.